

A 3-D Projection Model for X-ray Dark-field Imaging

Lina Felsner^{*,1,2}, Shiyang Hu^{*,1,3}, Andreas Maier^{1,2,3}, Johannes Bopp¹, Veronika Ludwig^{2,4}, Gisela Anton⁴, and Christian Riess¹

¹Pattern Recognition Lab, Department of Computer Science,

²International Max Planck Research School for Optics and Imaging,

³Erlangen Graduate School in Advanced Optical Technologies (SAOT),

⁴Erlangen Centre for Astroparticle Physics (ECAP),

Friedrich-Alexander University of Erlangen-Nuremberg, Erlangen, Germany

*Both authors contributed equally to this work

lina.felsner@fau.de, shiyang.hu@fau.de

ABSTRACT

The X-ray dark-field signal can be measured with a grating-based Talbot-Lau interferometer. It measures small angle scattering of micrometer-sized oriented structures. Interestingly, the signal is a function not only of the material, but also of the relative orientation of the sample, the X-ray beam direction, and the direction of the interferometer sensitivity. This property is very interesting for potential tomographically reconstructing structures below the imaging resolution. However, tomographic reconstruction itself is a substantial challenge.

A key step of the reconstruction algorithm is the inversion of a forward projection model. In this work, we propose a very general 3-D projection model. We derive the projection model under the assumption that the observed scatter distribution has a Gaussian shape.

We theoretically show the consistency of our model with existing, more constrained 2-D models. Furthermore, we experimentally show the compatibility of our model with simulations and real dark-field measurements. We believe that this 3-D projection model is an important step towards more flexible trajectories and, by extension, dark-field imaging protocols that are much better applicable in practice.

1 Introduction

The probably most studied acquisition system for X-ray phase-contrast imaging is the Talbot-Lau grating interferometer. This system allows to measure a X-ray absorption image and two additional images, namely the differential phase image and the dark-field image. The X-ray dark-field measures ultra-small angle scattering, which is caused by inhomogeneities in materials at micrometer scale¹⁻³.

Recently, X-ray dark-field imaging has received much attention for its potential applications in medical imaging and non-destructive material testing. The investigated applications in medical imaging span a wide range. Examples are the identification of different lung diseases⁴⁻⁷, lung cancer⁸, the identification of micro-calcifications⁹, or the differentiation of kidney stones¹⁰. Other examples are the detection of bone structures² and fractures¹¹ as well as brain connectivity¹². Also for material testing there are a wide range of application of the dark-field signal^{3,13-16}.

The origin of the observed dark-field can have various reasons, such as small-angle x-ray scattering, an intra-pixel differential phase contrast that cannot be resolved, or even beam hardening¹⁷. While the effects are not clearly separable, we will focus on the dark-field created through small-angle scattering. Two properties of the dark-field signal are particularly interesting. First, ultra-small angle scattering is caused by structural variations at the scale of few micrometers, which is significantly below the resolution of conventional X-ray imaging systems^{18,19}. Second, a grating-based system allows to measure the 3-D orientation of elongated micrometer-sized structures such as fibers²⁰. Traditional absorption X-ray systems have to be able to fully resolve a fiber in order to measure its orientation. In contrast to that, X-ray dark-field imaging enables to deduce the fiber orientation of considerably smaller structures.

Jensen *et al.*²¹ and Revol *et al.*²² explored the fundamentals of the dark-field orientation-dependency. In a tomographic setup, either the object or the imaging system rotates during the acquisition. During the rotation, the relative orientation between object and system changes, which leads to a variation in the signal. This signal variation allows to reconstruct the orientation of the structure. There have been several reconstruction methods proposed in previous works²³⁻²⁸. However all of them are based on 2-D projection models of the 3-D structure. This means that the models rely on the reconstruction of several 2-D slices and are not compatible with true 3-D trajectories.

In this work, we aim to overcome this limitation by proposing a dark-field projection model over the 3-D space. This allows

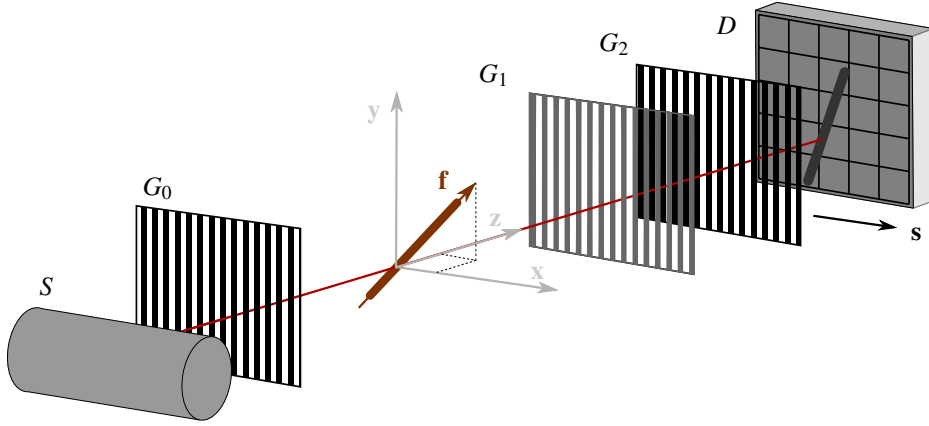


Figure 1. Sketch of an X-ray Talbot-Lau interferometer. The setup consists of a source S , a detector D , and three gratings G_0 , G_1 , and G_2 in between. The global coordinate system is denoted as x , y , z , an example fiber in the beam path is denoted as f , and the sensitivity direction of the setup is denoted as s .

to directly estimate the 3-D structure, and to use sophisticated 3-D trajectories such as a helix.

1.1 Talbot-Lau Interferometer

The Talbot-Lau interferometer is a grating-based phase-contrast setup. A sketch of the system is shown in Fig. 1. The system is an extension of conventional X-ray imaging setups, where three gratings G_0 , G_1 , and G_2 are placed between the source and detector. X-rays are generated by a conventional X-ray tube S . This X-ray tube can be operated in an X-ray regime that is compatible with medical applications, such that a medical X-ray detector D ^{29,30} can be used. Grating G_0 effectively separates X-rays from the large source into narrow slit sources that are individually coherent, but mutually incoherent. G_1 imprints a periodic phase modulation onto the wave front to create an interference pattern at the detector. Both gratings G_0 and G_1 have periods that are in the range of few micrometers. For operation with the much lower resolution of clinical X-ray detectors, the interference pattern is sampled with the G_2 grating in front of the detector, which also has a period in the range of micrometers. The sampling at the detector can be either performed by slightly detuning the grating G_2 , which leads to the Moiré effect^{31–33}, or by performing phase stepping^{29,30}. Both approaches sample points on the interference curve, which can then be fitted by a sine. In practice, two scans are performed, namely a reference scan without object in the beam path, and an object scan with the object. By comparing the sinusoidal curve of both scans, it is possible to calculate the three quantities absorption, differential phase, and dark-field. As in standard X-ray imaging, absorption is defined as the change in the average intensity. The differential phase is the angular shift of the sine. The dark-field signal is given by the ratio of the amplitude of the sine over the average intensity.

For this work, it is important to note that all three signals are created by sampling the sinusoidal function in one direction. We call this direction the *sensitivity direction* s . The sensitivity direction is perpendicular to the grating bars.

1.2 Related Work

X-ray Tomography is performed by rotating either the X-ray setup or the object during the acquisition. This rotation changes the orientation of the object relative to the sensitivity direction. A key difference between traditional X-ray absorption and dark-field is the impact of this relative orientation: X-ray absorption is independent of the relative orientation, while X-ray dark-field depends on it.

This makes a major difference for the choice of reconstruction algorithm. The popular filtered backprojection (FBP) algorithm implicitly assumes that the signal strength is independent of the viewing direction — which does in general not hold for X-ray dark-field imaging.

The tomographic reconstruction, in general, requires the inversion of a projection model. For the angle-dependent dark-field signal, several 2-D projection models were proposed, which are discussed briefly in the following.

Jensen *et al.*²¹ first showed the angle dependency of dark-field projections. They rotated the object around the optical axis of the system, and found that the variations in visibility can be described by the first two orders of the Fourier expansion. Shortly afterwards, Revol *et al.*²² modeled the dark-field scatter by a 2-D Gaussian function and showed that the logarithm of the dark-field signal can be formulated as

$$\tilde{V}(\omega) = A + B \cdot \sin^2(\omega - \theta) \quad , \quad (1)$$

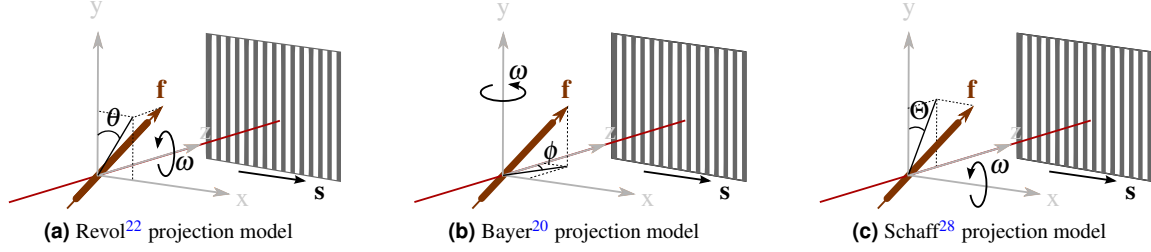


Figure 2. Sketch of three different 2-D projection models from previous works. The rotation angle is given as ω . The fiber vector is denoted as \mathbf{f} , and θ and ϕ are the elevation angle and azimuthal angle, respectively. \mathbf{s} is the sensitivity direction.

where ω is the rotation angle of the fiber around the optical axis, θ is the starting angle of the fiber in the \mathbf{xy} -plane (see Fig. 2a) and A, B are an isotropic and anisotropic contribution of the scatter, respectively. The projection models^{21,22} assume that the object is rotated around the optical axis, which limits these models to thin sample layers. Malecki *et al.*³⁴ investigated the signal formation for the superposition of layers with different fiber orientations. They conclude that the dark-field signal can be represented as the line integral along the beam direction over the anisotropic scattering components.

In order to describe the dark-field for thicker objects, Bayer *et al.*²⁰ proposed another projection model. They showed that the projection of a fibrous structure also depends on the azimuthal angle ϕ . This corresponds to the angle of the fiber projection in the \mathbf{xz} plane in Fig. 2b. They derive the dark-field signal as

$$\tilde{V}(\phi) = A + B \cdot \sin^2(\phi - \omega) \quad . \quad (2)$$

The third projection model was proposed by Schaff *et al.*²⁸ and is shown in Fig. 2c. Here, the grating bars are aligned along the 2-D trajectory, and the dark-field signal is measured along along the rotation axis. Schaff *et al.* approximate this signal as constant with respect to the tomographic rotation, such that the the scattering strength only depends on the angle between the fiber and the rotation axis.

This approximation simplifies the reconstruction, since a normal FBP algorithm can be used. However, for the two other projection models, the resulting signal per voxel varies along the trajectory. 2-D object orientations are in this case reconstructed via iterative reconstruction^{23–27}. Among these works, Bayer *et al.*²³ proposed a method to reconstruct 2-D in-plane orientations of fibers. Hu *et al.*²⁴ proposed to reconstruct the 3-D orientation by combining two 2-D in-plane scans with different trajectories. X-ray tensor tomography has been proposed by Malecki *et al.*²⁵, Vogel *et al.*²⁶, and Wiczczyk *et al.*²⁷ by combining multiple 2-D planes.

Since all projection models describe the dark-field only as a function of one angle, it is only possible to reconstruct a 2-D slice. The reconstruction of the full 3-D distribution of oriented materials requires the combination of scans from several trajectories, which overall leads to quite complex acquisition protocols. Malecki *et al.*²⁵ reconstructed a scattering tensor by using the model from Revol *et al.*²² and rotated the sample into a finite number of scattering directions. Hu *et al.*²⁴ used the model by Bayer *et al.*^{20,23} and used two 2-D reconstructions to compute the 3-D fiber direction, while Schaff *et al.*²⁸ fit a 3-D ellipse to individually reconstructed 2-D slices.

Previous works take different approaches to describe the 3-D nature of X-ray dark-field, ranging from Gaussian distributions²¹ over a kartesian basis²⁶ to a spherical harmonics basis²⁷. However, to our knowledge, there exists to date no direct 3-D reconstruction algorithm. One of the reasons for this may be the fact that a reconstruction method requires the inversion of a projection model, which to our knowledge has not been defined yet in 3-D.

The definition of a 3-D model makes it possible to use 3-D dark-field trajectories. For example, the helix is a popular 3-D trajectory with favorable properties in traditional absorption tomography. In this case, Tuy's condition for absorption image can be applied, and the completeness of such a certain trajectory can be shown³⁵. In principle, a similar system can be pursued for dark-field tomography if a well-described 3-D trajectory is available. As long as only 2-D trajectories can be used, the best known acquisition schemes that fully measure the scattering orientations are still quite complex³⁶.

1.3 Contributions and Organization of this Work

In this work, we propose a fully three-dimensional X-ray dark-field projection model. Previous works are limited to descriptions of 2-D projections of the dark-field signal, which limits the reconstruction to 2-D scatter projections, and constrains the trajectories to 2-D. In contrast, the proposed model enables the use of an arbitrary scanning geometry, and overcomes the need for combining several 2-D trajectories. The proposed model allows to use established 3-D scanning trajectories to acquire the

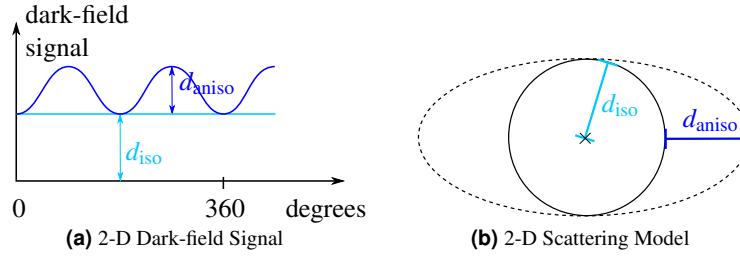


Figure 3. Isotropic (d_{iso}) and Anisotropic (d_{aniso}) parts for the 2-D dark-field signal and scattering model.

3-D scatter distribution, like for example a helical geometry. Furthermore, it enables the development of novel 3-D geometries that aim at optimizing the recovery of directional information for specific clinical examinations or visual inspection tasks.

Additionally, the proposed model is very general. It allows to freely choose the ray direction and the sensitivity direction. That way, it overcomes the restriction of earlier works to parallel beam geometries. Instead, it allows to model a cone beam, which is of major importance for many popular hardware designs, like for example a line scanner.

We only use the assumption that the scatter distribution of the dark-field signal is a 3-D Gaussian, and we derive the general projection model from that. Furthermore, we discuss the impact of additional constraints if they are available, and demonstrate the consistency with existing 2-D models. In the experiments, we show that the proposed model accurately fits predicted dark-field values from a wave simulation as well as from real experiments.

The paper is organized as follows. Section 2 provides a mathematical derivation of the proposed model, which describes the dark-field signal formation in a very general way. Afterwards, in Sec. 3, we discuss the impact of additional constraints on the model and show that our model is consistent with the 2-D projection models discussed in Sec. 1.2. Experiments that link the predicted signal to simulations and actual measurements are presented in Sec. 4. We conclude the paper in Sec. 5.

2 Proposed X-ray Dark-field Projection Model

The X-ray dark-field signal measures the X-ray small angle scattering of microstructures in a sample. X-ray dark-field scattering has the special property that its observed magnitude depends on the relative orientation of the sample in the setup. To characterize the signal, we use the notion of *isotropic* and *anisotropic* scattering components. This notion was originally introduced for 2-D projection models. A schematic sketch of this model is shown in Fig. 3. Here, the isotropic component scatters in all directions equally strongly, independent of the sample or setup orientation. Conversely, observations of scatter of the anisotropic component vary with the sample and setup orientation.

Thus, if a sample scatters purely isotropically, its signal is independent of the orientation. Such a signal can be reconstructed in a similar manner as X-ray absorption. However, if a sample exhibits partially anisotropic scatter, the signal formation depends on the orientation and thus becomes considerably more difficult to reconstruct. In particular, any algorithm for 2-D or 3-D reconstruction has to explicitly take the direction-dependent signal variation into account.

In order to model the signal formation, we introduce the notion of a *fiber*. A fiber is a microstructure that exhibits a mixture of isotropic and anisotropic scattering. The derivation of the model is organized as follows. First, we expose the relationship between a fiber and its associated scatter distribution in Sec. 2.1. In Sec. 2.2, we show how the fiber is projected by the X-ray onto the sensitivity direction. In Sec. 2.3, we show how the projected image of the fiber is converted to a scatter distribution. In Sec. 2.4, we state the complete model, which is the actually observed dark-field signature for a sample point. Afterwards, Sec. 2.5 shows how the measured signal is expressed as line integrals.

The dark-field signal formation depends on three quantities, namely the directions of the X-ray, the dark-field sensitivity direction, and the orientation of the fiber. We describe a very general model that considers all three quantities as arbitrary vectors in 3-D. This generality has several advantages. It allows us to model not only a system with parallel beam and a perpendicular sensitivity direction, but instead arbitrary acquisition geometries. Examples for such more general system designs are the use of a cone-beam scanning geometry, which influences the ray direction, or the use of a curved X-ray detector, which results in different sensitivity directions. It also allows to model a 3-D helical scanning trajectory, which requires flexibility in all these quantities.

2.1 Relationship between Fiber and Scatter Distribution

We make the simplifying assumption that a fiber has the shape of a cylinder. More specifically, the fiber cross section is assumed to be a circle, and the height of the cylinder is assumed to be at least as long as the radius of that circle. The isotropic scattering component is mainly determined by the radius of the circle. The anisotropic scattering component is connected to the size of the cylinder, and will be more rigorously defined in Sec. 2.3.

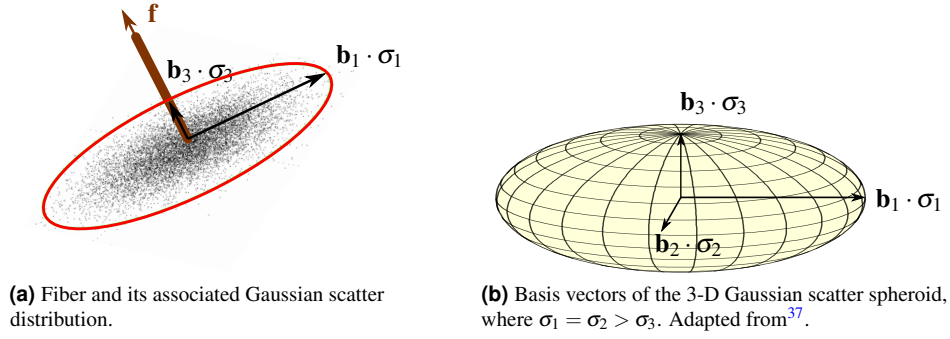


Figure 4. Illustrations of the 3-D Gaussian scatter distribution.

Mathematically, we represent a fiber as a 3-D vector \mathbf{f} in \mathbb{R}^3 , where the vector is parallel to the cylinder axis. The observed fiber creates dark-field scatter. Scatter is not deterministic, and therefore commonly described as a distribution.

For the following discussion, we are only interested in the relative orientations of the fiber and its associated scatter. Thus, without loss of generality, we assume that a fiber and its scatter distribution are rooted in the origin of the coordinate system. We assume that the shape of a fiber scatter distribution is a 3-D Gaussian $g(\mathbf{x})$, which is in line with earlier models on 2-D scatter distributions²¹. Then,

$$g(\mathbf{x}) = \frac{1}{\sqrt{(2\pi)^3 |\Sigma|}} \cdot \exp\left(-\frac{1}{2}(\mathbf{x}^\top \Sigma^{-1} \mathbf{x})\right), \quad (3)$$

where Σ denotes the 3×3 covariance matrix. The shape of $g(\mathbf{x})$ is completely described by Σ .

We make the mild assumption that this covariance matrix Σ can be diagonalized (which is satisfied for any non-trivial 3-D Gaussian scatter observation). Then, the eigenvalues of Σ describe the scatter strength with respect to its eigenbasis spanned by the eigenvectors $\mathbf{b}_1, \mathbf{b}_2, \mathbf{b}_3$. The eigenvalues correspond to the variances, i.e., the squared standard deviations along each principal axis of the distribution:

$$\Sigma = \begin{pmatrix} \sigma_1^2 & 0 & 0 \\ 0 & \sigma_2^2 & 0 \\ 0 & 0 & \sigma_3^2 \end{pmatrix}. \quad (4)$$

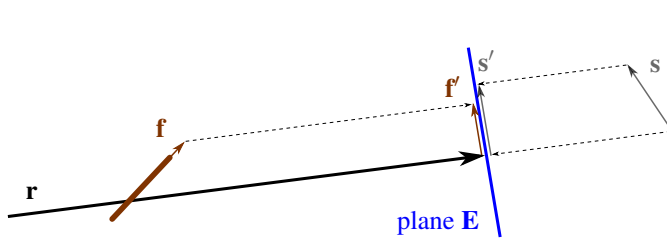
These variances have a special distribution, which comes from the particular case of a scattering fiber: the main scattering direction of the fiber is the 2-D subspace that is perpendicular to \mathbf{f} . This is illustrated in Fig. 4a. All scatter directions within this 2-D subspace are indistinguishable. As a consequence, the two largest eigenvalues σ_1^2 and σ_2^2 are identical, i.e., $\sigma_1^2 = \sigma_2^2$. The weakest scattering is observed in the direction of \mathbf{f} , which is quantified by the smallest eigenvalue $\sigma_3^2 \leq \sigma_1^2$. This is illustrated in Fig. 4a. The eigenvector \mathbf{b}_3 is associated with the smallest eigenvalue σ_3^2 and parallel to \mathbf{f} . More specifically, both vectors are identical with the exception that their sign might be flipped, i.e., $\mathbf{b}_3 = \pm \mathbf{f}$. The restrictions on the eigenvalues induces that the shape of the scattering function is a oblate spheroid. A 3-D sketch of the eigenvalues is shown in Fig. 4b.

2.2 3-D Fiber Projection Model

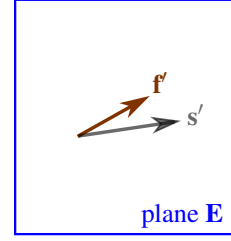
The dark-field signal formation depends on three geometric vectors, namely the direction of the X-ray, the dark-field sensitivity direction, and the orientation of the fiber. Ultimately, we seek the projection of the fiber along the ray direction onto the sensitivity direction. This is a mapping from the 3-D fiber vector onto a (1-D) scalar value. A non-parallel X-ray projection, e.g. from a cone beam, is modelled by a rotation of the fiber. The sensitivity direction can have an arbitrary orientation in space. To relate the fiber direction and the sensitivity direction, we introduce a virtual plane that is perpendicular to the X-ray. Both the fiber and the sensitivity direction are projected onto that plane. Then, the 2-D projection of the fiber onto the sensitivity direction in the plane is performed. The resulting equations show that the plane cancels, and that the projection of the fiber onto the sensitivity direction can be written as a scalar product. The mathematical details are presented below.

Let us consider a single fiber vector \mathbf{f} . Without loss of generality, this fiber is located in the origin of our world coordinate system. The X-ray dark-field projection ray \mathbf{r} passes through that fiber, and thereby also the origin of the coordinate system.

In imaging systems, all X-rays that form one projection are typically modelled as either parallel or diverging from a central ray \mathbf{c} . This changes the relative orientation between \mathbf{r} and the fiber vector \mathbf{f} . To correct for the diverging ray, we denote the angle of divergence as α , and rotate the fiber in the plane spanned by \mathbf{c} and \mathbf{r} in the opposite direction. The corresponding rotation matrix is denoted as \mathbf{R}_α . In the case of parallel projection, \mathbf{R}_α is the 3×3 identity matrix.



(a) Sketch of the projection of vector \mathbf{f} and \mathbf{s} on the plane \mathbf{E} . Please note, that this sketch does not match the exact mathematical description, since the plane \mathbf{E} does not lie in the origin.



(b) Planar view on the plane \mathbf{E} with the projected vectors \mathbf{f}' and \mathbf{s}' .

Figure 5. Projection of the fiber direction and the sensitivity direction onto the plane.

We project the fiber \mathbf{f} onto a plane \mathbf{E} that is perpendicular to the X-ray direction \mathbf{r} . For this projection, we use orthogonal projections instead of perspective projections of the scatter pattern. This is possible, because the projection of a fiber signature onto the detector is in the range of micrometers, but a single detector pixel is typically two orders of magnitude larger.

An orthogonal projection of a 3-D vector onto a plane can be performed with an inner product between the vector and a transformation matrix consisting of the 3-D coordinates of the 2-D basis. We define the 2-D projection plane as a plane where \mathbf{r} is the normal vector. Since \mathbf{r} passes through the origin, we find it convenient to choose the plane to also pass through the origin, i.e.,

$$\mathbf{E} = (\mathbf{r}_1^{\text{ortho}}, \mathbf{r}_2^{\text{ortho}}) \quad , \quad (5)$$

with $\mathbf{E} \in \mathbb{R}^{3 \times 2}$ where $\mathbf{r}_1^{\text{ortho}}$ is a vector perpendicular to \mathbf{r} , i.e., $\mathbf{r}^\top \mathbf{r}_1^{\text{ortho}} = 0$, and $\mathbf{r}_2^{\text{ortho}} = \mathbf{r} \times \mathbf{r}_1^{\text{ortho}}$ is the second vector spanning the plane, also perpendicular to \mathbf{r} . This projection is visualized in Fig. 5a.

The projection of the fiber along the ray and onto the 2-D plane \mathbf{E} is then given as product of the rotated fiber \mathbf{f} with \mathbf{E} , i.e.,

$$\mathbf{f}' = (\mathbf{R}_\alpha \mathbf{f})^\top \mathbf{E} \quad , \quad (6)$$

where $\mathbf{f}' \in \mathbb{R}^2$ is now a two-dimensional vector in the plane \mathbf{E} .

The sensitivity direction \mathbf{s} denotes the direction along which the X-ray dark-field signal can be measured. It is a 3-D vector with an arbitrary orientation. To relate the fiber with the sensitivity direction, we also project \mathbf{s} onto plane \mathbf{E} . Analogously to the fiber-plane projection, we also use here an orthogonal projection. The 2-D projection of \mathbf{s} on \mathbf{E} is

$$\mathbf{s}' = \mathbf{s}^\top \mathbf{E} \quad . \quad (7)$$

The projection of both vectors \mathbf{f}' and \mathbf{s}' on \mathbf{E} are shown in Fig. 5b.

To determine the alignment of the fiber \mathbf{f} with sensitivity direction \mathbf{s} , the inner product is computed, i.e.

$$\mathbf{f}'' = \mathbf{f}'^\top \cdot \mathbf{s}' \quad (8)$$

$$= \left((\mathbf{R}_\alpha \mathbf{f})^\top \mathbf{E} \right)^\top \cdot (\mathbf{s}^\top \mathbf{E}) = \left(\mathbf{E}^\top (\mathbf{R}_\alpha \mathbf{f}) \right) \cdot (\mathbf{s}^\top \mathbf{E}) \quad . \quad (9)$$

Equation 9 can be simplified by noting that the inner product commutes, which leads to

$$\mathbf{f}'' = \left(\mathbf{s}^\top \mathbf{E} \right) \cdot \left(\mathbf{E}^\top (\mathbf{R}_\alpha \mathbf{f}) \right) \quad (10)$$

$$= \mathbf{s}^\top \cdot (\mathbf{R}_\alpha \mathbf{f}) \quad , \quad (11)$$

since $\mathbf{E} \mathbf{E}^\top = \mathbf{I}$. Equation 11 shows that the projection of the fiber through the system onto the sensitivity direction reduces to directly computing the inner product between the fiber and the sensitivity direction.

Note that in the case of a cone beam, the rotation of the fiber by \mathbf{R}_α can also be replaced by a rotation of the sensitivity direction \mathbf{s} in the opposite direction. While we believe that the rotation of the fiber \mathbf{f} is more intuitive, it may be preferable for an actual implementation of a reconstruction algorithm to rotate the sensitivity direction \mathbf{s} , since \mathbf{s} is a given quantity from the setup geometry, and \mathbf{f} is the unknown variable.

2.3 3-D Projection Model for Scattering

The projection of the fiber onto the sensitivity direction can be translated into the projection of the scatter. The scatter is the actually observed quantity in the imaging system. The inverse of this conversion links the observations to the unknown fiber direction.

As discussed in Sec. 2.1 the scatter distribution for a given fiber \mathbf{f} is given as

$$\mathbf{f} \mapsto \begin{pmatrix} \sigma_1^2 & & \\ & \sigma_2^2 & \\ & & \sigma_3^2 \end{pmatrix} (\mathbf{b}_1 \ \mathbf{b}_2 \ \mathbf{b}_3) , \quad (12)$$

where $\sigma_1^2 = \sigma_2^2$, and $\mathbf{b}_1, \mathbf{b}_2, \mathbf{b}_3$ are an orthogonal basis.

In Sec. 2.2 we considered the transformation from the 3-D fiber to a 1-D signal. We now want to describe this transformation for the scattering distribution. Since the distribution is described by an orthogonal basis, we can transform the basis vectors \mathbf{b}_i individually to get the transformation.

Since we defined our projection for an arbitrary fiber \mathbf{f} , we can use the same mapping for each basis vector \mathbf{b}_i . The measured projection of the scattering component i is then given as

$$\sigma_i^{2''} = \mathbf{s}^\top \cdot (\mathbf{R}_\alpha (\sigma_i^2 \mathbf{b}_i)) \quad (13)$$

$$= \sigma_i^2 \cdot (\mathbf{s}^\top \cdot (\mathbf{R}_\alpha \mathbf{b}_i)) . \quad (14)$$

Under the consideration that the scattering distribution is symmetric, the variance may not depend on the sign of the basis vectors \mathbf{b}_i , and its oscillation has to be of period π . In analogy to previous 2-D models^{22,23}, both requirements are addressed by squaring the inner product. The projected variance is thus

$$\hat{\sigma}_i^{2''} = \sigma_i^2 \cdot (\mathbf{s}^\top \cdot (\mathbf{R}_\alpha \mathbf{b}_i))^2 . \quad (15)$$

2.4 Complete 3-D Dark-Field Projection Model

With the individual projections of the fiber and the scattering distribution at hand, we combine both in this section to directly describe the scatter distribution for a given fiber. To this end, we use the introduced notions of *isotropic* and *anisotropic* scattering. The isotropic part results in an equal amount of scatter in all directions, while the anisotropic part depends on the relative orientation of the fiber, ray direction, and sensitivity direction. The goal is to describe the 1-D dark-field scattering signal in dependency of the fiber, since the fiber is the quantity that shall eventually be reconstructed.

The observed dark-field signal is modeled as

$$d = d_{\text{iso}} + d_{\text{aniso}} \left(\mathbf{s}^\top (\mathbf{R}_\alpha \mathbf{f}) \right)^2 . \quad (16)$$

Here, we again square the scaling factor of the anisotropic part to resemble the fact that the signal has a period of π instead of 2π . Analogously, the amount of isotropic and anisotropic scattering is also defined over the variances of the 3-D scattering function. Thus, the isotropic component is given as

$$d_{\text{iso}} = \sigma_1^2 = \sigma_2^2 , \quad (17)$$

while the anisotropic component is

$$d_{\text{aniso}} = -(\sigma_1^2 - \sigma_3^2) . \quad (18)$$

To define the anisotropic component as the subtraction from the isotropic scattering may appear counter-intuitive at first glance. However, it allows to directly represent the fiber \mathbf{f} in the model. We believe that it is useful for building a reconstruction algorithm on top of the model to have the fiber direction directly accessible, since it is the primary quantity of interest.

The derivation to use the fiber vector in the of Eq. 16 comes from the projected variance in Eq. 15. If we consider the smallest scattering component, we observe

$$\hat{\sigma}_3^{2''} = \sigma_3^2 \cdot (\mathbf{s}^\top \cdot (\mathbf{R}_\alpha \mathbf{b}_3))^2 . \quad (19)$$

Since the eigenvector \mathbf{b}_3 and the fiber vector \mathbf{f} are collinear, we can substitute \mathbf{b}_3 in Eq. 19 by \mathbf{f} . This leads to

$$\hat{\sigma}_3^{2''} = \sigma_3^2 \cdot (\mathbf{s}^\top \cdot (\mathbf{R}_\alpha \mathbf{f}))^2 , \quad (20)$$

which is used to get the dark-field model in Eq. 16.

In 2-D models, the isotropic component is defined as the amount that scatters in all directions equally, while the anisotropic component is defined as an additional component in the direction perpendicular to the fiber direction. In 3-D, a direct adaptation of this approach is somewhat more complicated, since the additional scatter of the fiber perpendicular to its main axis forms a 2-D subspace. We argue that the concept of isotropic and anisotropic components is not really transferable to the 3-D case. In 3-D, one can interpret Eq. 16 as the reduction of observed scatter in the direction of the main axis of the fiber, which is mathematically correct, yet somewhat counter-intuitive.

The projection of the dark-field does not only depend on the scattering strength described in Eq. 16, but also on the length of the projection rays through the fiber. Since the fiber is assumed to be smaller than one pixel, the dark-field per voxel \mathbf{x} can be expressed as:

$$d(\mathbf{x}) = C(\mathbf{f}, \alpha, \sigma_1, \sigma_3) \cdot d, \quad (21)$$

where $C(\mathbf{f}, \alpha, d_{\text{iso}}, d_{\text{aniso}})$ is a function describing the average length through the fiber cylinder, dependent on the fiber direction, the ray direction and linked to isotropic and anisotropic values.

2.5 Dark-Field Line Integrals

In standard X-ray projection imaging, the measured signal intensity is the line integral along the X-ray beam line L . Malecki *et al.*³⁴ showed that the superposition of dark-field signals results in a line integral along the beam direction. The dark-field signal is similar to the absorption signal given by

$$D_L = \exp \left[- \int_L d(\mathbf{x}) dL \right]. \quad (22)$$

Here, the line integral is only influenced by the object geometry.

To make the dark-field more interpretable and achieve a non-linear intensity transformation as oftentimes used in X-ray absorption processing, several authors use $-\log(D_L)$ ³⁸.

3 Impact of Additional Constraints on the Model

The proposed projection model is very general. In this section we will show how specific assumptions allow for simplifications. In particular, we show that the model is consistent with the more constrained 2-D projection models by Revol²², Bayer²⁰, and Schaff²⁸. We will now show that we are consistent with these if we constrain our model to parallel beams and a circular 2-D trajectory. As sketched in Fig. 2, we define for all three 2-D models the sensitivity direction as $\mathbf{s} = (1, 0, 0)^\top$.

In a parallel beam geometry, the rotation matrix \mathbf{R}_α simplifies to the identity, i.e., $\mathbf{R}_\alpha = \mathbb{1}$. Consequently, the anisotropic component only depends on the relative orientation of the fiber and sensitivity direction, thus

$$d = d_{\text{iso}} + d_{\text{aniso}} (\mathbf{s}^\top \mathbf{f})^2. \quad (23)$$

Revol *et al.* rotates the fiber around the ray direction. Thus, the fiber orientation of \mathbf{f} in the \mathbf{xy} plane depends on the starting angle θ and the rotation angle ω . We will denote this dependency as $\mathbf{f}(\omega)$. The fiber is then given as

$$\mathbf{f}(\omega) = \begin{pmatrix} \cos(\omega - \theta) & -\sin(\omega - \theta) & 0 \\ \sin(\omega - \theta) & \cos(\omega - \theta) & 0 \\ 0 & 0 & 1 \end{pmatrix} \begin{pmatrix} f_x \\ f_y \\ f_z \end{pmatrix}, \quad (24)$$

with $\mathbf{f} = (f_x, f_y, f_z)^\top$. The dark-field model thus becomes $d = d_{\text{iso}} + d_{\text{aniso}} ((1, 0, 0)\mathbf{f}(\omega))^2$, which can be transformed into the original formulation $A + B \cdot \sin^2(\omega - \theta)$.

The mapping to the model by Bayer *et al.* can be performed in a similar manner. Here, the fiber is rotated around the \mathbf{y} -axis. Then,

$$\mathbf{f}(\omega) = \begin{pmatrix} \cos(\phi - \omega) & 0 & \sin(\phi - \omega) \\ 0 & 1 & 0 \\ -\sin(\phi - \omega) & 0 & \cos(\phi - \omega) \end{pmatrix} \begin{pmatrix} f_x \\ f_y \\ f_z \end{pmatrix}, \quad (25)$$

which results in the original formulation $A + B \cdot \sin^2(\phi)$.

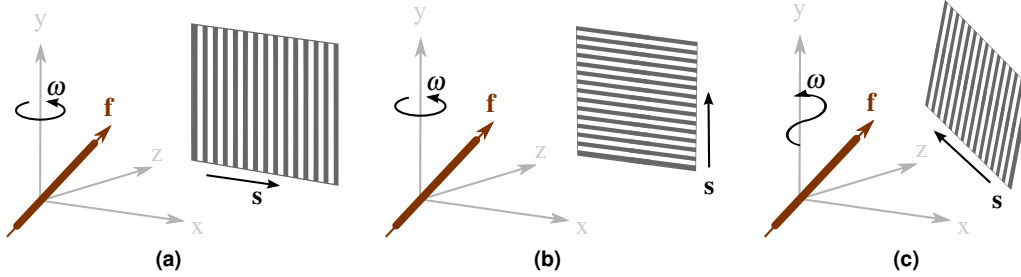


Figure 6. Three different trajectories to evaluate the dark-field projection model (Sec. 4.1). (a, b) Circle trajectory. (c) Helical trajectory. The sensitivity direction s is shown for each scanning mode.

The model by Schaff *et al.* constrains the sensitivity direction parallel to the rotation axis. Then, the projection of the fiber vector (as stated in Eq. 11) is given as

$$\mathbf{f}(\omega)'' = (1, 0, 0) \begin{pmatrix} 1 & 0 & 0 \\ 0 & \cos(\omega - \Theta) & -\sin(\omega - \Theta) \\ 0 & \sin(\omega - \Theta) & \cos(\omega - \Theta) \end{pmatrix} \begin{pmatrix} f_x \\ f_y \\ f_z \end{pmatrix} = f_x, \quad (26)$$

which is constant. It is interesting to note, however, that the model does not consider variations in intersection lengths through the fiber. In practice, the signal is only then approximately constant, if the fiber exhibits only a small elevation angle. In this case, the intersection length is nearly identical for different rotation angles ω .

In summary, the proposed model can be transformed into each of the three existing 2-D models with the addition of suitable constraints. At the same time, however, the proposed model is general enough to also represent a full 3-D space with an arbitrarily oriented X-ray, fiber, and sensitivity.

4 Experiments and Results

In this section we experimentally evaluate the proposed 3-D dark-field projection model. We sequentially evaluate different aspects of the model, to mitigate the combinatorial complexity of evaluating the full parameter space. The evaluated aspects of the model are

1. Dark-field projection model (Equation 16)
2. Dark-field signal of a single fiber (Equation 21)
3. Dark-field measurements (Equation 22).

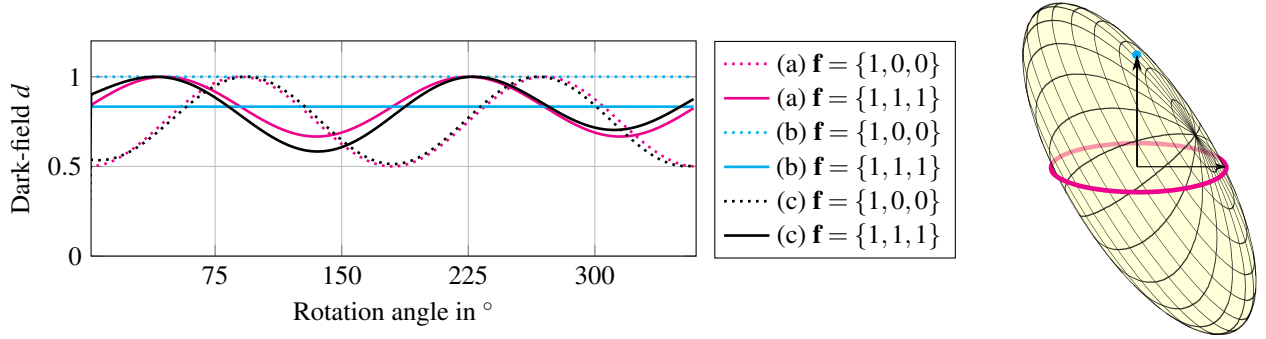
The corresponding experiments are described and discussed in the sections 4.1, 4.2, and 4.3, respectively. To evaluate the proposed projection model, we compare the results to simulated and real dark-field signals in Sec 4.2 and 4.3.

4.1 Dark-field Projection Model

The formulation of the dark-field in Eq. 16 is sufficiently flexible to describe different trajectories and sensitivity directions. In this experiment, we show the dependency of the dark-field on the X-ray direction and sensitivity direction. To this end, we simulate three different trajectories as shown in Fig. 6. We evaluate the dark-field for two different fiber vectors, both with larger scattering coefficient $\sigma_1 = \sigma_2 = 1$ and smaller scattering coefficient $\sigma_3 = 0.5$. The fiber directions are $\mathbf{f} = \{1, 0, 0\}$ and $\mathbf{f} = \{1, 1, 1\}$, respectively.

All three trajectories have a source-isocenter distance of 600 mm and source-detector distance of 1200 mm. We simulate two circular 2-D trajectories over 360° with an angular increment of 1.5° . Both trajectories have different sensitivity directions. The sensitivity direction s for trajectory (a) in Fig. 6 can be represented by the vector $\{1, 0\}$ in the detector plane and lies therefore in the rotation plane. Trajectory (b) in Fig. 6 has the sensitivity direction along the rotation axis, i.e. the vector $\{0, 1\}$ in the 2-D detector plane. The third trajectory (c) is a helical 3-D trajectory, also with an angular increment of 1.5° and a pitch $h = 0.5$. The sensitivity direction is aligned with the helical trajectory. The sensitivity direction is in all cases always chosen perpendicularly to the projection ray in order to not introduce an additional scaling factor from the inner product in Eq. 16.

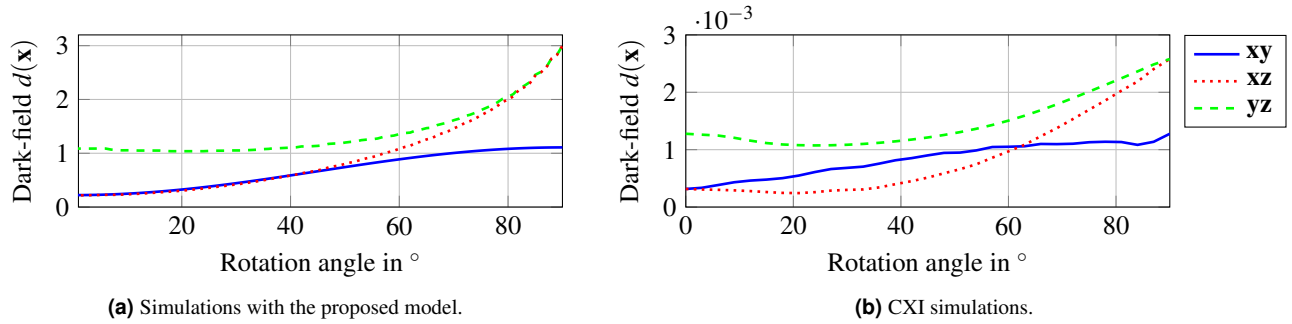
The resulting dark-field signals are shown in Fig. 7a over the rotation angle ω . In magenta, the dark-field signals for both fibers on the circular trajectory (a) are shown. They oscillate with a regular sinusoidal. The fiber that lies within the rotation



(a) Line plot of dark-field for different trajectories and fiber vectors. The corresponding grating orientations are shown in Fig. 6 and $\sigma_1 = 1$, $\sigma_3 = 0.5$.

(b) Projected vectors shown on the spheroid for the fiber vector $\mathbf{f} = \{1, 1, 1\}$. Magenta is the trajectory (a). Light blue shows the signal for trajectory (b).

Figure 7. Projections of the dark-field projection model from Eq. 16 according to the trajectories in Fig. 6.



(a) Simulations with the proposed model.

(b) CXI simulations.

Figure 8. Dark-field signals (Eq. 21) for the rotation of a fiber in the three planes spanned by the axes of the coordinate system. (a) generated signal with the proposed model. (b) wavefront simulations.

plane (magenta, dotted line) reaches the minimum and maximum theoretically possible dark-field values. The elevated fiber (magenta, solid line) creates an overall stronger signal that, due to the elevation, never reaches the minimum. This is also illustrated in the example scattering spheroid in Fig. 7b. Here, the magenta circumference indicates the measured scatter intersection for trajectory (a) for the elevated fiber vector $\mathbf{f} = \{1, 1, 1\}$.

For the second 2-D trajectory (b), the sensitivity direction is aligned with the rotation axis. As shown in the light blue lines in Fig. 7a, this results in a constant signal for both fiber directions. In this case, the elevated fiber $\mathbf{f} = \{1, 1, 1\}$ (solid, light blue) creates a weaker signal. The scattering strength of the elevated fiber is shown as a light blue dot on the spheroid in Fig. 7b.

The most complex trajectory is the helical 3-D trajectory (trajectory (c) in Fig. 6). The dark-field signals for both fibers are shown in black in Fig. 7a. Due to the constant change in angle between the fiber and the sensitivity direction, the signal change is not symmetric over the 360° . While this observation holds for both fibers, it is more pronounced for fiber vector $\mathbf{f} = \{1, 1, 1\}$ (solid black line).

The experiments demonstrate how the dark-field signal depends on the X-ray direction and the sensitivity direction. Furthermore, the experiment also shows that the dark-field signal behaves differently for 2-D and 3-D trajectories. These differences in the predicted signals demonstrate the need of a 3-D projection model for performing a true 3-D reconstruction.

4.2 Dark-field Signal of a Single Fiber

To verify the proposed dark-field signal for a complete fiber (Eq. 21), we compare it to numerical simulations. We simulate the dark-field with a simulation framework for coherent X-ray imaging (CXI) from Ritter *et al.*³⁹. The setup parameters for the simulation are chosen as follows. The G_1 is placed at 0.01 m, with a period of 4.37×10^{-6} m, a height of 5×10^{-6} m and a duty-cycle of 0.5. The G_2 is placed at 0.17 m, with a period of 2.4×10^{-6} m, a height of 300×10^{-6} m and a duty-cycle of 0.5. Both gratings are simulated as gold. The detector is positioned immediately behind G_2 . The size of the focal spot is set to

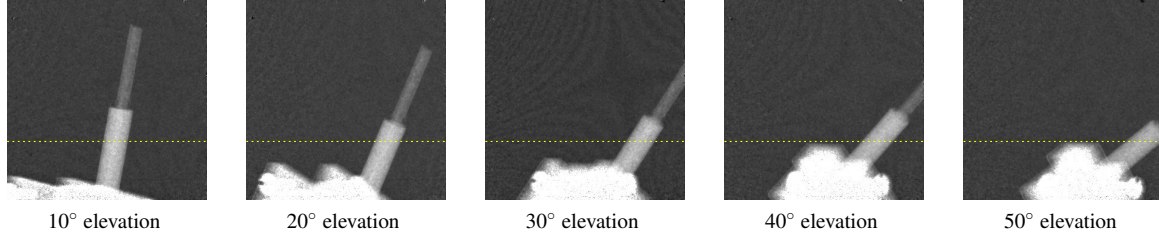


Figure 9. Carbon-rods at different elevation angles. First projection image with a windowing between -0.31 and $+1.0$. For the measured dark-field signal we used the central pixels of the rod along the yellow, dashed line.

$10\ \mu\text{m}$, and the pixel width is set to $50\ \mu\text{m}$. The design energy of the system is $25\ \text{keV}$. The simulated object is a teflon fiber (PTFE) with a radius of $1.79\ \mu\text{m}$ and a length of $15\ \mu\text{m}$.

We set the fiber parameters in the model to the eigenvalues $\sigma_1 = 1.5$ and $\sigma_2 = 0.3$, which correspond to the teflon fiber parameters.

The negative logarithm of the simulated signal is shown in Fig. 8. Figure 8a shows the result with our model, while Fig. 8b shows the result from the CXI simulations. The dark-field signals are shown in the three planes spanned by the coordinate system, namely xy -, xz -, and yz -plane. Overall, the proposed model and the wavefront simulations agree very well. The different magnitude between the two signals simulations, are due to the range chosen parameter spaces for the experiments.

The signal in the xy -plane (blue, solid line) changes only slightly in both simulations. In this plane, the change between the larger and the smaller scatter eigenvalues is observed. While our model leads to a distinct sinusoidal change (Fig. 8a), it is more noisy for the CXI simulation (Fig. 8b) due to numerical instabilities.

The dark-field signal in the xz - and yz -plane (red and green lines, respectively) increases with the rotation angle ω , i.e., with increasing inclination of the fiber into the beam direction. Equation 16 predicts for such an inclination no increase, but instead a constant signal. However, the reason for the increasing signal lies in the increased intersection length of the ray through the fiber, as denoted in Eq. 21. It is also interesting to note that this increase is even stronger than the difference of the scatter eigenvalues. The green signal that shows the yz -plane is affected by both effects, the scattering eigenvalues and intersection length through the fiber. Overall, the wavefront simulations and the predicted values of the proposed model agree very well.

4.3 Dark-field Measurements

We show that the proposed complete projection model (Eq. 22) also agrees with experimentally obtained dark-field measurements. The real data consists of a carbon fiber reinforced polymer rod with a diameter of $4\ \text{mm}$. The fiber was measured at five different tilting (elevation) angles, namely 10 , 20 , 30 , 40 , and 50° . A projection image at each angle is shown in Fig. 9. For each tilting angle, 100 projection images are taken over a rotation of 180° at $40\ \text{kVp}$ and $40\ \text{mA}$. The measurements were performed with a Siemens MEGALIX CAT Plus 125/40/90-125GW medical X-ray tube using a tungsten anode. The used X-ray flat panel detector was a PerkinElmer Dexela 1512 with $74.8\ \mu\text{m}$ pixel pitch, running in 2×2 binning mode for processing a faster read-out resulting in a $150\ \mu\text{m}$ pixel pitch. For each projection 30 phase-steps with $0.1\ \text{s}$ acquisition time were used. The gratings have a period of $24.39\ \mu\text{m}$ for G_0 , $2.18\ \mu\text{m}$ for G_1 , and $2.4\ \mu\text{m}$ for G_2 . The setup is $1.854\ \text{m}$ long, with a $G_0 - G_1$ distance of $1473\ \text{mm}$, a $G_1 - G_2$ distance of $142\ \text{mm}$, and a $G_0 - \text{object}$ distance of $1118\ \text{mm}$. The dark-field is given as $-\log(V/V_{\text{ref}})$. For the extracted dark-field signal we used the central pixels of the rod along the yellow, dashed line in Fig. 9.

To simulate the dark-field of the carbon rod, we have to estimate the corresponding parameters. We simulated the dark-field signal of the rod with a diameter of $40\ \text{pixel}$ and used scatter parameters $\sigma_1 = 1.4$ and $\sigma_3 = 1$. However, since the real measurements bring along a lot of other unknown parameters, such as the number of fibers within the rod, the dark-field values are not quantitatively comparable.

Figure 10 shows the dark-field signal of the fiber over 180° around the y -axis for different elevation angles, where an elevation angle of 0° represents a fiber that is aligned with the rotation axis. The sensitivity direction is aligned with the rotation plane. Figure 10a shows the dark-field simulations, while Fig. 10b shows the real dark-field measurements. Please note, that the rod were not aligned perfectly parallel to the detector plane on the beginning, which leads to shift in the rotation angle. The simulations are in very good agreement with the real dataset. In both cases, the signal fluctuation increases with increasing tilting angle of the fiber. The influence of the path length of the projection ray through the object can be seen in the non-regular fluctuation along the rotation angles. As a sidenote, the noise in the plot showing the real data corresponds to the overall noise level of the setup. This can be observed in Fig. 9 in the image background.

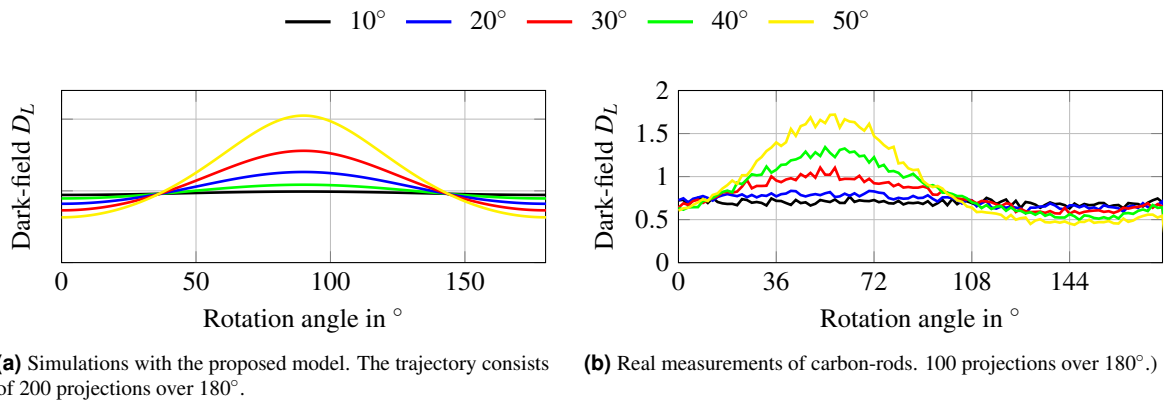


Figure 10. Dark-field signal of carbon-rods with a diameter of 4 mm.

5 Conclusions and Outlook

In this paper, we propose a X-ray dark-field imaging projection model. It explicitly calculates structural quantities in 3-D using the direction of the fiber, the ray direction and the sensitivity direction. To our knowledge, this is the first true 3-D dark-field model.

We believe that this model is a powerful tool for further development of X-ray dark-field imaging. In contrast to existing (2-D) projection models, where the imaging trajectory is pre-defined, our model allows to image arbitrary 3-D trajectories, like for example a helical trajectory. The proposed model is very general, but by addition of suitable constraints it can be curbed to any of the existing 2-D models. We evaluated the consistency of the model with itself, with a wave-front simulation, and with experimental dark-field measurements. In future work, we will investigate an algorithm for X-ray dark-field reconstruction that can make full use of 3-D trajectories.

Acknowledgements

The authors acknowledge funding from the German Research Foundation (DFG).

Project DFG GZ: AN 257/21-1 | MA 4898/6-1.

L.F and V.L are supported by the International Max Planck Research School for Optics and Imaging.

Author Contributions Statement

S.H. and A.M. conceived the model. S.H. developed the initial theoretical framework. L.F. and C.R. expanded the theoretical framework. L.F. performed the experiments and analyzed the data. J.B. carried out the wavefront simulations. V.L. and G.A. performed the real data measurements. L.F., S.H., and C.R. wrote the paper with input from all authors.

Additional Information

Competing interests. The authors declare no competing interests.

References

1. Pfeiffer, F. *et al.* Hard-X-ray dark-field imaging using a grating interferometer. *Nature Materials* **7**, 134–137 (2008).
2. Wen, H., Bennett, E. E., Hegedus, M. M. & Rapacchi, S. Fourier X-ray scattering radiography yields bone structural information. *Radiology* **251**, 910–918 (2009).
3. Revol, V. *et al.* Laminate fibre structure characterisation by orientation-selective X-ray grating interferometry. In *Proceedings of the 5th Conference on Industrial Computed Tomography*, 45–51 (2014).
4. Weber, T. *et al.* Investigation of the signature of lung tissue in X-ray grating-based phase-contrast imaging. *arXiv preprint arXiv:1212.5031* (2012).
5. Yaroshenko, A. *et al.* Visualization of neonatal lung injury associated with mechanical ventilation using X-ray dark-field radiography. *Scientific Reports* **6**, 24269 (2016).

6. Hellbach, K. *et al.* In vivo dark-field radiography for early diagnosis and staging of pulmonary emphysema. *Investigative Radiology* **50**, 430–435 (2015).
7. Hellbach, K. *et al.* Depiction of pneumothoraces in a large animal model using X-ray dark-field radiography. *Scientific Reports* **8**, 2602 (2018).
8. Scherer, K. *et al.* X-ray dark-field radiography-in-vivo diagnosis of lung cancer in mice. *Scientific Reports* **7**, 402 (2017).
9. Michel, T. *et al.* On a dark-field signal generated by micrometer-sized calcifications in phase-contrast mammography. *Physics in Medicine & Biology* **58**, 2713 (2013).
10. Scherer, K. *et al.* Non-invasive differentiation of kidney stone types using X-ray dark-field radiography. *Scientific Reports* **5**, 9527 (2015).
11. Hauke, C. *et al.* Hairline fracture detection using talbot-lau X-ray imaging. In *Medical Imaging 2018: Physics of Medical Imaging*, vol. 10573, 105734F (International Society for Optics and Photonics, 2018).
12. Wiczorek, M. *et al.* Brain connectivity exposed by anisotropic X-ray dark-field tomography. *Scientific reports* **8** (2018).
13. Reza, S. *et al.* Investigation on the directional dark-field signals from paperboards using a grating interferometer. *Journal of Instrumentation* **9**, C04032 (2014).
14. Ludwig, V. *et al.* Non-destructive testing of archaeological findings by grating-based X-ray phase-contrast and dark-field imaging. *Journal of Imaging* **4**, 58 (2018).
15. Yang, F. *et al.* Dark-field X-ray imaging of unsaturated water transport in porous materials. *Applied Physics Letters* **105**, 154105 (2014).
16. Prade, F. *et al.* Nondestructive characterization of fiber orientation in short fiber reinforced polymer composites with X-ray vector radiography. *NDT & E International* **86**, 65–72 (2017).
17. Koenig, T. *et al.* On the origin and nature of the grating interferometric dark-field contrast obtained with low-brilliance X-ray sources. *Physics in Medicine & Biology* **61**, 3427 (2016).
18. Yashiro, W., Terui, Y., Kawabata, K. & Momose, A. On the origin of visibility contrast in X-ray talbot interferometry. *Optics Express* **18**, 16890–16901 (2010).
19. Revol, V. *et al.* Sub-pixel porosity revealed by X-ray scatter dark field imaging. *Journal of Applied Physics* **110**, 044912 (2011).
20. Bayer, F. *et al.* Projection angle dependence in grating-based X-ray dark-field imaging of ordered structures. *Optics Express* **21**, 19922–19933 (2013).
21. Jensen, T. H. *et al.* Directional X-ray dark-field imaging of strongly ordered systems. *Physical Review B* **82**, 214103 (2010).
22. Revol, V., Kottler, C., Kaufmann, R., Neels, A. & Dommann, A. Orientation-selective X-ray dark field imaging of ordered systems. *Journal of Applied Physics* **112**, 114903 (2012).
23. Bayer, F. L. *et al.* Reconstruction of scalar and vectorial components in X-ray dark-field tomography. *Proceedings of the National Academy of Sciences of the United States of America* **111**, 12699–12704 (2014).
24. Hu, S. *et al.* 3-D tensor reconstruction in X-ray dark-field tomography — the first phantom result. In *Bildverarbeitung für die Medizin*, 492–497 (2015).
25. Malecki, A. *et al.* X-ray tensor tomography. *Europhysics Letters* **105**, 38002 (2014).
26. Vogel, J. *et al.* Constrained X-ray tensor tomography reconstruction. *Optics Express* **23**, 15134–15151 (2015).
27. Wiczorek, M., Jud, C., Schaff, F., Pfeiffer, F. & Lasser, T. X-ray tensor tomography - a linear system approach to reconstruction. In *Proceedings of the 4th International Meeting on image formation in X-ray CT*, 25–8 (2016).
28. Schaff, F., Prade, F., Sharma, Y., Bech, M. & Pfeiffer, F. Non-iterative directional dark-field tomography. *Scientific Reports* **7**, 3307 (2017).
29. Pfeiffer, F., Weitkamp, T., Bunk, O. & David, C. Phase retrieval and differential phase-contrast imaging with low-brilliance X-ray sources. *Nature Physics* **2**, 258–261 (2006).
30. Weitkamp, T., David, C., Kottler, C., Bunk, O. & Pfeiffer, F. Tomography with grating interferometers at low-brilliance sources. In *Proceedings of the SPIE — Developments in X-ray Tomography*, vol. 6318, 63180S–1 (2006).
31. Takeda, M., Ina, H. & Kobayashi, S. Fourier-transform method of fringe-pattern analysis for computer-based topography and interferometry. *Journal of the Optical Society of America A* **72**, 156–160 (1982).

32. Bennett, E. E., Kopace, R., Stein, A. F. & Wen, H. A grating-based single-shot X-ray phase contrast and diffraction method for in vivo imaging. *Medical Physics* **37**, 6047–6052 (2010).
33. Bevins, N., Zambelli, J., Li, K., Qi, Z. & Chen, G.-H. Multicontrast X-ray computed tomography imaging using talbot-lau interferometry without phase stepping. *Medical Physics* **39**, 424–428 (2012).
34. Malecki, A. *et al.* Coherent superposition in grating-based directional dark-field imaging. *PloS One* **8**, e61268 (2013).
35. Maier, A., Kugler, P., Lauritsch, G. & Hornegger, J. Discrete estimation of data completeness for 3-D scan trajectories with detector offset. In *Bildverarbeitung für die Medizin 2015*, 47–52 (Springer, 2015).
36. Sharma, Y., Schaff, F., Wiczorek, M. J., Pfeiffer, F. & Lasser, T. Design of acquisition schemes and setup geometry for anisotropic X-ray dark-field tomography (AXDT). In *Scientific Reports* (2017).
37. Ruen, T. Spheroids. <https://commons.wikimedia.org/wiki/File:Spheroids.svg> (2017). Accessed on 2019-01-28.
38. Bech, M. *et al.* Quantitative X-ray dark-field computed tomography. *Physics in Medicine & Biology* **55**, 5529 (2010).
39. Ritter, A. *et al.* Simulation framework for coherent and incoherent X-ray imaging and its application in talbot-lau dark-field imaging. *Optics Express* **22**, 23276–23289 (2014).